

# Heat Transfer And Pressure Drop Of An Angled Discrete Turbulator At Elevated Reynolds Numbers Up To 900,000

**Sam Ghazi-Hesami**

Polytechnique Montréal  
Montréal, Québec, Canada, H3T 1J4  
sam.ghazi-hesami@polymtl.ca  
(Siemens Energy Canada Ltd,  
sam.ghazi-hesami@siemens-energy.com)

**Dylan Wise**

The University of Oxford  
Oxford, Oxfordshire, UK, OX2 0ES

**Keith Taylor**

Siemens Energy Canada Ltd  
Montréal, Québec, Canada, H9P 1A5

**Peter Ireland**

The University of Oxford  
Oxford, Oxfordshire, UK, OX2 0ES

**Étienne Robert**

Polytechnique Montréal  
Montréal, Québec, Canada, H3T 1J4

## Abstract

Turbulators are a promising avenue to enhance heat transfer in a wide variety of applications. An experimental and numerical investigation of heat transfer and pressure drop of a broken V (chevron) turbulator is presented at Reynolds numbers ranging from approximately 300,000 to 900,000 in a rectangular channel with an aspect ratio (width/height) of 1.29. The rib height is 3% of the channel hydraulic diameter while the rib spacing to rib height ratio is fixed at 10. Heat transfer measurements are performed on the flat surface between ribs using transient liquid crystal thermography.

The experimental results reveal a significant increase of the heat transfer and friction factor of the ribbed surface compared to a smooth channel. Both parameters increase with Reynolds number, with a heat transfer enhancement ratio of up to 2.15 (relative to a smooth channel) and a friction factor ratio of up to 6.32 over the investigated Reynolds number range. Complementary CFD RANS (Reynolds-Averaged Navier-Stokes) simulations are performed with the  $\kappa$ - $\omega$  SST turbulence model in ANSYS Fluent® 17.1, and the numerical estimates are compared against the experimental data. The results reveal that the discrepancy between the experimentally measured area averaged Nusselt number and the numerical estimates increases from approximately 3% to 13% with increasing Reynolds number from 339,000 to 917,000. The numerical estimates indicate turbulators enhance heat transfer by interrupting the boundary layer as well as increasing near surface turbulent kinetic energy and mixing.

*Key words: heat transfer, rib, turbulator, broken V, transient liquid crystal thermography, high Reynolds number*

# 1 Introduction

The enhancement of convective heat transfer through surface features has been investigated in a variety of applications such as the thermal design of electronics, solar air heaters and gas turbines. The use of turbulators, for instance taking the shape of transverse or angled ribs, is a passive approach that can be implemented for this purpose. These ribs enhance heat transfer by disrupting the boundary layer as well as by increasing surface area, flow turbulence and mixing [1]. This turbulator induced improvement of heat transfer is often accompanied by increased pressure drop compared to a smooth channel. This balance of heat transfer and pressure loss augmentations, of a ribbed channel compared to a smooth one, is commonly used to quantify thermal performance, often at a constant pumping power.

Most studies of turbulator performance are carried out at Reynolds numbers ( $Re$ ) lower than 100,000. However, in recent years, investigations at higher Reynolds number (up to 400,000-550,000) have been published for a variety of geometries, revealing a strong dependence of the heat transfer and pressure drop on the turbulator shape and channel Reynolds number for gas turbine components such as the combustion chamber and turbine blades [2-7]. Recently, Mhetras et al. [8] conducted turbulator heat transfer studies at very high Reynolds numbers up to 1,300,000 for application on gas turbine combustors. The maximum target Reynolds number in the current investigation is 917,000. The broken V configuration is considered in the following, as it has shown promise in studies realized at a wide range of Reynolds numbers [8-11], providing advantages in terms of heat transfer and thermal performance. Therefore, a unique combination of turbulator and test channel geometric parameters is investigated up to a maximum target Reynolds number of 917,000 to provide additional data points in the design space investigated by the previous authors.

The present investigation aims to assess the heat transfer on a broken V ribbed plate at elevated Reynolds numbers, particularly above 300,000, and increase the understanding of the aerodynamic features responsible for the measured thermal performance. To complement experimental measurements of surface heat transfer, the general features of the flow field are examined using CFD simulations. The numerical work presented has two objectives. First to further assess the performance of the  $k-\omega$  SST turbulence model at very high Reynolds numbers by comparing numerical results against experiments. Second, to provide a qualitative understanding of the flow field characteristics responsible for the observed behaviour of the heat transfer and friction factor, as the Reynolds number is increased.

The state of the art for high Reynolds number turbulator studies for heat transfer enhancement is presented in the next section, followed by description of the experimental and numerical approaches implemented. Results covering the Reynolds number range of 339,000 to 917,000 are then presented and discussed.

The objective of the current study is to provide a detailed measurement of heat transfer coefficient on a broken V rib-roughened plate over a wide range of Reynolds numbers. These experimental results are then compared to numerically estimated Nusselt number values. A qualitative description of the flow field is also provided using the numerical estimates. Recommendations for further improvements of the broken V turbulator configuration are finally drawn, as well as recommendations for the experimental and numerical investigation.

## **2 Literature Review and State of the Art**

When considering the performance of turbulators on surfaces, a variety of parameters such as the rib angle, size, spacing, channel geometry and Reynolds number may affect the heat transfer and friction factor. Additionally, for numerical studies, the Reynolds-Averaged Navier-Stokes (RANS) approach is typically used and its implementation for the problem at hand will also be discussed in this section. Finally, the experimental technique used in our experiments for measuring the surface heat transfer coefficient, transient liquid crystal thermography, will also be discussed as it has a strong influence on the nature and quality of the results. In the present work, the rib height ( $e$ ) and spacing (pitch,  $P$ ) are normalized by the test channel hydraulic diameter ( $e/D_h$  ratio) and rib height ( $P/e$  ratio) respectively, based on conventions found in the literature.

### **2.1 Experimental Work**

The effect of the turbulator angle relative to that of the flow on heat transfer and friction factor has been studied by various authors notably Kim et al. [12] and Han et al. [10, 13, 14]. Surfaces with oblique parallel ribs are reported to provide additional heat transfer compared with 90° ribs, i.e. perpendicular to the flow [12-14]. For example, Han et al. [13] assessed the aerothermal performance of 90°, 60°, 45° and 30° ribs, with angled ribs showing potential for greater heat transfer augmentation than 90° ribs for Reynolds numbers of 10,000 to 60,000. However, the results of Han and Park [15] indicated that the channel aspect ratio influences the effectiveness of the rib angle and the resulting Nusselt number distribution.

Han and Zhang [10] also examined the influence of discretizing or breaking the ribs into segments along their length, on the heat transfer and pressure drop. They compared ribbed walls with continuous and broken parallel and V shaped ribs at Reynolds numbers of 15,000 to 90,000 at  $e/D_h$  ratio of 0.0625 and  $P/e$  ratio of 10. They concluded that the broken V ribs

at  $60^\circ$  provided the highest heat transfer augmentation on the ribbed wall. The increased heat transfer associated with breaking the V configuration was attributed to the likely creation of additional secondary flow structures and increased turbulence level near the ribbed wall compared with the continuous V configuration. Additional measurements and flow visualization were however recommended to verify this hypothesis. In this study, as in many others, an increase of the Reynolds number resulted in the decrease of the effect of the ribs, as measured by the Nusselt number augmentation compared with a smooth channel. The friction factor ratio however did not exhibit much sensitivity to the Reynolds number for the broken rib configurations.

The results from Maurer et al. [4] for continuous V ribs showed the global trend for the heat transfer augmentation at high Reynolds number seems to be a levelling off for  $Re > 200,000$ , with  $e/D_h = 0.02$  while a small increase is still observed for larger ribs with  $e/D_h = 0.0625$ . However, as the friction factor increased more rapidly than the heat transfer coefficient with Reynolds number, the thermal performance at constant pumping power declined for all cases. These experiments were performed at Reynolds numbers between 95,000 and 500,000 in a rectangular channel with ribs at a  $P/e$  ratio of 10. The optimum thermal performance at constant pumping power was achieved with shorter ribs ( $e/D_h = 0.02$ ) indicating the potential advantage of short ribs over tall ribs when minimizing pressure loss is crucial. Although the experiments of Kiml et al. [12] and Han et al. [10, 13-15] were performed in channels with two opposite ribbed walls, Maurer et al. [4] examined channels with both ribs on one side and also on two opposite sides.

Gupta et al. [9] and SriHarsha et al. [11] studied experimentally the effect of the broken V rib spacing ( $P/e$  ratio) and height ( $e/D_h$  ratio) in a square channel on the Nusselt number distribution and friction factor augmentation. The ribs had a square cross section and the Reynolds numbers were varied between 10,000 and 30,000. In the study by Gupta et al. [9], the  $P/e$  ratio, for a constant  $e/D_h$  ratio of 0.0625, did not have a significant effect on the average Nusselt number augmentation. However, SriHarsha et al. [11] observed that an increase of  $e/D_h$ , at a  $P/e$  ratio of 10, had an adverse effect. They also studied the effect of introducing a cavity between the wall surface and the rib (partial rib detachment from the wall on which it is mounted), noting an adverse effect on both heat transfer and friction factor. Mhetras et al. [8] investigated the aerothermal characteristics of a  $45^\circ$  angled broken V configuration, with a rib height to channel height ratio of 0.11 and  $P/e$  ratio of 10, in a large aspect ratio channel ( $AR=6$ ) and reported deterioration of heat transfer augmentation and thermal performance with increasing Reynolds number.

The previous studies indicate superior heat transfer and thermal performance can be obtained using complex turbulator configurations such as the broken V. However, as the performance of these ribs depends on their size, angle and flow

Reynolds number, the current investigation examines the performance of a unique broken V configuration at elevated Reynolds numbers where published data is scarce.

## 2.2 Numerical Studies and RANS Modelling

When addressing such complex fluid mechanic problems, numerical simulations can provide insight into flow characteristics. However, the reliability of the numerical approach must be evaluated by comparing against experimental data. The capabilities of RANS models to estimate the heat transfer associated with turbulators has been assessed by several researchers including Maurer et al. [4], Promvonge et al. [16] and Tang and Zhu [17]. RANS based simulations provide a cost-effective means of estimating aerodynamic characteristics by modelling of turbulence parameters and closing the Reynolds stress terms. However, RANS models are not universal and a turbulence model cannot deliver accurate results for all types of flow fields and applications [18]. Several studies show that the solution provided by RANS models depends on the turbulence model implemented, examples of which are presented by Tang and Zhu [17] and Lörstad [3]. On the other hand, the LES (Large Eddy Simulation) technique resolves large turbulence scales and models the more universal small scales leading to enhanced accuracy over a broad range of applications. The advantages of the LES approach come at a significant computational cost, explaining the current prevalence of RANS models for performing CFD simulations in a timely manner with limited resources. It is therefore imperative to examine the performance of RANS models against experimental data. Maurer et al. [4] used a two-layer  $\kappa$ - $\epsilon$  model and reported noticeable underprediction of heat transfer and friction factor for the majority of simulated configurations and Reynolds numbers. Tang and Zhu [17] studied a unique configuration of broken parallel angled, V and W type ribs, with sloped sides, at Reynolds numbers between 5,500 and 16,000. The comparison of the  $\kappa$ - $\omega$  SST and  $\kappa$ - $\epsilon$  RNG models showed that the former provides better agreement with experimental data. Choi et al. [19] reported good agreement between experimental Nusselt number distribution of parallel angled ribs and numerical estimates using the  $\kappa$ - $\omega$  turbulence model. The  $\kappa$ - $\omega$  SST turbulence model was also selected by Chaube et al. [20] due to its good performance in assessing turbulator heat transfer.

Promvonge et al. [16] performed simulations of the experiments performed by SriHarsha et al. [11] using the  $\kappa$ - $\epsilon$  RNG turbulence model and reported close agreement of the numerically estimated Nusselt number (Nu) distribution, except for areas of flow attachment and separation. On average, the numerical data slightly underpredicted the experimental heat transfer results. They also evaluated the effect of thinning the rib cross section from a square to a rectangular shape as well as increasing the rib height. This had the effect of increasing both Nusselt number and friction factors, following a postulated

augmentation of the turbulence intensity and vortex size. The results revealed a decline of the thermal performance with increasing Reynolds number for both square and thin ribs.

The numerical studies of Maurer et al. [4] were performed at Reynolds numbers an order of magnitude higher than those of the previously cited references [16, 17, 19, 20]. The current investigations report discrepancies between RANS simulations and experimental data, especially at high Reynolds numbers. The work presented here therefore aims to gather high Reynolds number experimental measurements of the Nusselt number distribution and compare the results against numerical calculations (section 5). The  $\kappa$ - $\omega$  SST turbulence model was selected due its good performance in the studies presented above.

### **2.3 Heat Transfer Measurement**

A broad review of the techniques available to measure heat transfer coefficients over a surface is provided by Han et al. [21], covering techniques such as liquid crystal thermography, infrared thermography and naphthalene sublimation. While liquid crystal (LC) and infrared thermography methods determine heat transfer via direct measurement of surface temperature, the naphthalene sublimation technique estimates indirectly the local heat transfer, through the amount of substance that is removed over a surface exposed to convection. The current investigation was performed using the transient liquid crystal technique. This technique can provide accurate surface temperature measurements, within one degree Celsius or less, with high spatial resolution over the coated surface [22, 23]. Liquid crystal thermography may also offer a cost advantage compared with infrared thermography [22]. Additionally, heat transfer measurement techniques using temperature sensitive surface coatings have been used and refined in recent decades at University of Oxford, with examples of earlier works by Clifford et al. [24] and Byerley et al. [25]. Liquid crystal thermography allows for a contour of the surface temperature, depicting the thermal footprint of the flow near the surface. Therefore, it can be used to understand and hypothesize flow structures dominating the ribbed wall especially when combined with numerical modelling. Since temperature as well as thermal gradients affect the thermo-mechanical stresses and consequently the life of the component (e.g., in gas turbine applications), it is imperative to obtain high resolution map of heat transfer coefficient to calculate thermal stresses. Since high-resolution spatial distribution of heat transfer coefficient is not always available in the literature, the current study extends current knowledge by providing such detailed data for the broken V turbulator configuration at high Reynolds numbers.

### 3 Experimental Configuration and Method

#### 3.1 Ribbed Surface Description

The aerothermal characteristics of a broken V turbulator is investigated in a stationary straight channel fitted with a heater mesh upstream of the test section allowing for sudden changes in the temperature of the air flow over the ribbed surface. The rib shape and angle studied somewhat resemble the configurations of Gupta et al. [9] and SriHarsha et al. [11], however we consider a much higher Reynolds number with a  $0.0757 \cdot D_h$  gap between the side wall and the ribs (Fig. 1 & Fig. 2).

The test plate is located on one side (width) of the channel as displayed in Fig. 3(a). Boundary layer development occurs over the distance between the heater mesh and the first rib. In our experiments, this distance is  $4.35 \cdot D_h$  and it should be chosen to match the characteristics of the boundary layer in the application considered. For a fully developed flow, the entrance length is estimated to be  $43.37 \cdot D_h$  at  $Re=917,000$  ( $Re$  based on channel hydraulic diameter) following Munson et al. [26]. Due to limitations in laboratory space (University of Oxford), the effect of a longer entry length could not be investigated experimentally, and a numerical assessment of this parameter is recommended in a future investigation. The ribs have a square cross section and the investigated section coated in liquid crystal consists of 10 rows (5 sets), as depicted in Fig. 1(a). The turbulator dimensional characteristics are presented in Table 1 and Fig. 1(b). Each pair of rows is referred to as one segment as shown in Fig. 2. Inspired by the experimental data of SriHarsha et al. [11], indicating an improvement of heat transfer and thermal performance parameters for the broken V configuration when reducing the  $e/D_h$  ratio from 0.15 to 0.0625 at  $P/e$  ratio of 10, it was decided to further reduce the  $e/D_h$  to 0.03 for our experiments, while keeping the same  $P/e$  ratio of 10. The decision of using shorter ribs is reinforced by similar observed improvements in thermal performance, at constant pumping power, reported for continuous V ribs, by reducing the  $e/D_h$  ratio from 0.0625 to 0.02 [4]. In the current configuration, the repetitive detachment of the near surface flow leads to a boundary layer that is thinner than the characteristic lengths of the vortical structures set up by the ribs.

A total of 10 rib rows or 5 segments were placed on the test plate. The heat transfer coefficients were averaged for segments 3 and 4, allowing for the first 2 rib segments to start the secondary flow induced by the angled and discrete nature of the ribs. The objective was to also achieve a nearly established pattern of Nusselt number distribution (thermal periodicity) on the downstream rib segments.

**Table 1: Test configuration**

Rib type	Rib angle ( $\alpha$ )	P/e	e/D <sub>h</sub>	Re <sub>Dh</sub> = $\frac{\rho u D_h}{\mu}$
Broken V (Chevron)	60°	10	0.03	339,000-917,000

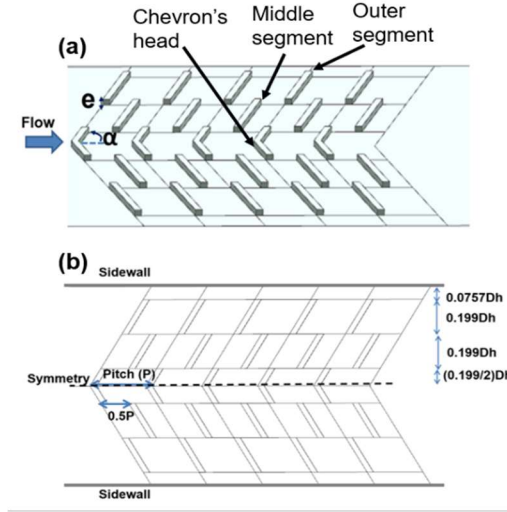


**Fig. 1: Rib arrangement, angle, and height (a) geometric dimensions (b)**

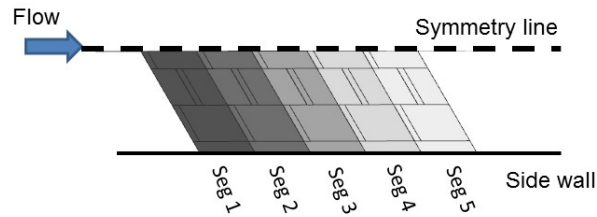


**Fig. 2: Geometrical segments used for discussion and heat transfer averaging**

### 3.2 Wind Tunnel Experimental Set up

The wind tunnel consists of a stainless-steel bell mouthed atmospheric inlet with a flow straightener followed by a heater mesh, used to induce a step change in the inlet flow temperature (Fig. 3). The bell-mouthed inlet reduces the cross-sectional area by a factor of 4. The wind tunnel is operated in suction mode and the heater mesh has a very fine structure, minimizing wind tunnel inlet turbulence entering the test section. Three of the walls of the test area are made of wood (medium density fiberboard) with the fourth being the replaceable 20 mm thick acrylic glass test plate (Perspex®). The nominal conductivity

values for Perspex® and medium density fiberboard are 0.19 (W/(m.K)) and 0.14 (W/(m.K)), respectively. The Perspex® test plate (mounted only on one wall) contains the investigated turbulator configuration. This material was selected due to its ease of manufacturing, low thermal conductivity and good transparency for optical access. The transition region following the heater mesh is insulated with a low conductivity material (Rohacell®) to minimise heat loss from the fluid prior to entering the test section. The heater mesh, made from stainless steel, has a wire diameter of 40  $\mu\text{m}$  and an aperture size of 63  $\mu\text{m}$  and is powered by a DC power supply with capacity of 150 kW. The air flow (up to  $\approx 6.2 \text{ m}^3/\text{s}$ ) is induced and controlled by an axial fan at the exit of the wind tunnel. An aluminium diffuser connects the test section to the blower. The test section has a hydraulic diameter ( $D_h$ ) of 0.384 m.

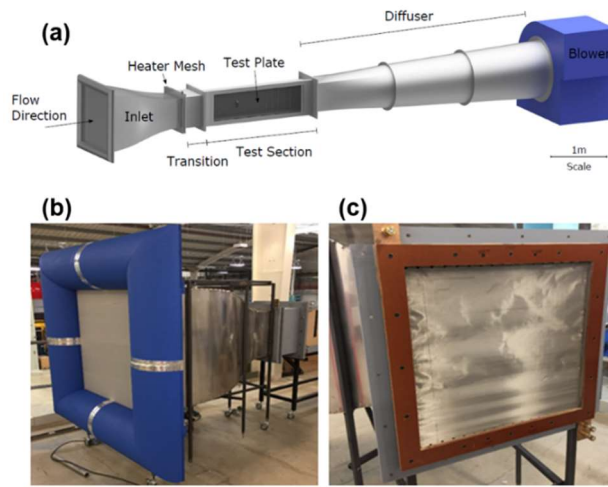


**Fig. 3: Wind tunnel arrangement (a), bell mouthed inlet (b), heater mesh (c)**

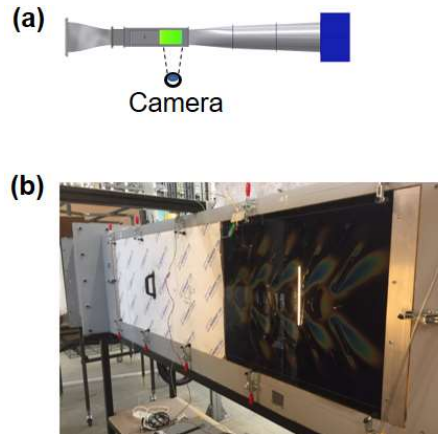


**Fig. 4: Camera position outside of rig (a) view of test section from outside while heater mesh is turned on (b)**

### 3.3 Heat Transfer Measurement/Calculation

The heat transfer between the flow and the rib surface was measured using transient liquid crystal thermography under atmospheric conditions. Narrow band liquid crystals displaying a full-scale colour change over a 1°C band were used and covered in black coating to improve visibility and contrast [27, 28]. This temperature sensitive layer is therefore sandwiched between the transparent test plate and the black coating, with a camera positioned to capture the liquid crystal response from outside the rig (Fig. 4). The process of calculating HTC is performed using a Matlab code [29] that converts the response of the liquid crystal to its equivalent temperature at each pixel and subsequently yields Nusselt number values, for each pixel as described by Ireland et al. [23, 30]. To perform this calculation and to characterize the phenomena in the test section, the information that must be obtained in the experiments are channel centreline temperature, pressure, and temporal history of wall surface temperature during the experiment. Radiation effects are neglected due to the low temperatures in the current experiment.

The centreline temperature of the test section flow is measured using T-type thermocouples on the channel centreline, above the ribbed surface. There are only small variations for the centreline temperature between the inlet and the outlet, because of the short length of the test section and insulating characteristic of the channel walls during the short test. Therefore, the centreline temperature, measured by a thermocouple over the ribs, was used as the reference temperature for heat transfer calculations. The approach of taking a single centreline temperature value is expected to be sufficient for the current experiment with a short channel and negligible variation of centreline temperature over the ribbed plate. However, for longer channels, various methods of HTC calculation based on local fluid temperature are available as discussed by Tsang [31]. The HTC at the channel surface is expressed by Eq. (1), where  $T_{ref-air}$  represents the centreline temperature over the ribbed surface. The Nusselt number is calculated using Eq. (2).

$$\dot{Q} = hA(T_{ref-air} - T_{wall}) \quad (1)$$

$$Nu = \frac{hD_h}{k_{air}} \quad (2)$$

A perturbation analysis is used to assess the constant odds uncertainty considering input errors associated with the instrumentation uncertainties. This method and its application in a liquid crystal experiment is described by Byerley [32] with reference to the work of Moffat [33]. For the results presented here, overall uncertainties in the HTC range from +/-9.0 to

+/-10.7% when increasing the Reynolds number from 300,000 to 900,000. This total uncertainty is calculated as the square root of sum of the squares of each contributing uncertainty. The maximum value of +/-10.7% estimated from the following: 3.3% from the initial temperature, 3.3% from the temperature rise, 5.1% from the thermal product, 8.2% from the calibration and 0.4% from video time offset. The friction factor measurement uncertainty is estimated to be within +/-4%.

### 3.4 Pressure Drop and Mass Flow Measurement

The pressure is measured at about one rib spacing (P) upstream and 1.6\*P downstream of the first and last ribs at the channel centreline, to avoid disturbing the flow over the ribs. 2D fields of static and total pressure were also taken at the same location downstream of the last rib and perpendicular to the free stream using a four-hole traverse probe. The diameter of the four-hole probe used is less than 1% of channel hydraulic diameter. The velocity upstream of the probe is determined through the pressure measurements at the four taps of the probe. The characteristics of this pressure probe and the measurement technique are described in detail by Tsang [31]. The friction factor is then calculated using the centreline static pressure measurements, following Eq. (3). Pressure drop measurements are performed in unheated flow (isothermal) conditions similar to the approach of Han et al. [13].

$$f = \frac{(\Delta p / L) D_h}{2 \rho u^2} \quad (3)$$

Where L represents the distance between the most upstream and downstream ribs, therefore the length over which the maximum flow disturbance and consequently pressure drop occurs. “u” is the average channel velocity ahead of the ribs. The friction factor in a smooth channel was estimated using the Blasius formulation Eq. (4). The friction factor from the ribbed channel is normalized by the smooth channel friction factor (Blasius correlation) to quantify the pressure penalty of the ribbed channel compared with a smooth tube.

$$f_0 = 0.046 \text{Re}^{-0.2} \quad (4)$$

The Nusselt number in a fully developed smooth duct, estimated by the Dittus-Boelter correlation Eq. (5), is used to normalize the experimentally obtained Nusselt number values. For comparison against the Dittus-Boelter correlation in a

fully developed smooth channel with heated inlet flow, the Nusselt number ratios can be scaled by multiplying the values by

$$\frac{Pr^{0.4}}{Pr^{0.3}}$$

$$Nu_0 = 0.023Re^{0.8}Pr^{0.4} \quad (5)$$

Velocity and consequently mass flow through the wind tunnel were calculated using the measurements of a pitot-static probe at the channel centreline upstream of the first rib.

## 4 Numerical Analysis

The numerical results were obtained using the commercially available finite volume solver ANSYS Fluent® 17.1. Turbulent transport modelling is critical for heat transfer. Therefore, to model the effects of turbulence, the  $\kappa$ - $\omega$  SST model of Menter [34] was used. The model blends the ability of the  $\kappa$ - $\omega$  model to reproduce near-wall flow behaviour and the ability of the  $\kappa$ - $\epsilon$  model in the free stream regions. Menter [34] provides a detailed description of the  $\kappa$ - $\omega$  SST formulation and showed good agreement of the numerical estimates and the experimental data for flows with adverse pressure gradients and separation. A summary of the theory is also available in the ANSYS Fluent® theory guide [35].

Convergence was achieved in an iterative manner via the SIMPLE algorithm for pressure and velocity coupling. The spatial discretization of the convective term was carried out using the second order upwinding technique for momentum, energy, turbulent kinetic energy and specific dissipation rate, while a second order method was used for pressure. Normalized error residuals as well as relevant quantities (HTCs, total pressure drop variation across ribs, near wall velocity) were monitored to judge convergence. For the  $\kappa$ - $\omega$  SST model to work properly, a fine mesh is generally required at the wall. As will be shown in the following sections, a  $y^+$  of  $\sim 1$  was achieved. Accordingly, no wall functions were applied, and the boundary layer was fully resolved. A standard value (0.85) for turbulent Prandtl number was used.

### 4.1 Boundary Conditions

A mass flow inlet with a uniform velocity profile was applied at the inlet of the computational domain, which approximately represents the uniform flow velocity and temperature exiting the heater mesh shortly downstream of the wind tunnel inlet. The outlet was  $5.4 \times P$  downstream of the last rib with a pressure outlet boundary condition set to atmospheric pressure. The

model outlet was located far downstream of the last rib to avoid outlet flow reversal in the simulations and minimize the effect of uncertainties in the outlet boundary conditions on the upstream flow. The ribbed walls were assigned a constant wall temperature, similar to the approach of Dhopade et al. [36], while adiabatic conditions were applied for the top and side walls. A no-slip boundary condition was imposed on all walls and the air is considered an incompressible ideal fluid, since the Mach number does not exceed 0.2. The specific heat, thermal conductivity and viscosity of air were calculated with a linear interpolation between the maximum and minimum temperatures in the wind tunnel. This approximation was deemed sufficient due to the small  $\Delta T$  of 14-15 K between the walls and the heated air. Although the numerical cases presented were run at the experimental  $\Delta T$  of 14-15 K ( $T_{\text{wall}}=293\&294$  K and  $T_{\text{inlet-air}}=308$  K), a sensitivity analysis was performed at Reynolds numbers of 339,000 and 917,000 where the wall temperature was increased by 5 K, reducing the  $\Delta T$  by nearly 33%. Negligible changes in the Nusselt number distribution indicated that the heat flux to the wall is dominantly proportional to the  $\Delta T$  while the Nusselt number distribution remains unchanged for the range of aerodynamic conditions and temperatures considered.

Due to the symmetric nature of the geometry, a symmetric model of the wind tunnel and the ribbed wall was created to reduce computational cost. The boundaries are depicted in Fig. 5 except for the top wall which runs parallel to the ribbed walls.

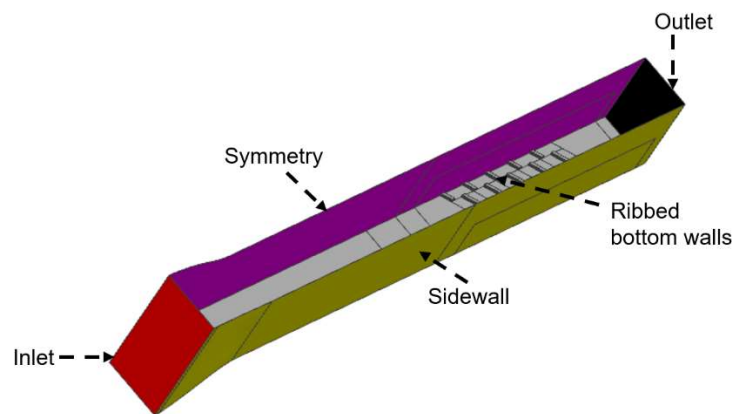


**Fig. 5: Boundaries**

## 4.2 Grid Generation

The wind tunnel model was divided into 2 zones, a high density mesh region around the ribbed plate and a medium density region for the rest (Fig. 6(a)). The high-density mesh area covers up to 6\*e above the ribbed walls. This volume was chosen after preliminary analysis on a coarse mesh indicated this volume to contain the highest gradients of velocity and turbulent kinetic energy. The ANSYS meshing tool with the Cut-Cell algorithm was used due to its robustness, optimized handling of element count and smooth aspect ratio transition. The volume immediately around the ribs and the entrance region of the wind tunnel contained the highest and lowest mesh densities respectively. All walls however were covered with 25 inflation layers, at an inflation rate of 1.2, to better capture the boundary layer development (Fig. 6(b)). Mesh sensitivity analysis was performed on the volumes surrounding the ribs to ensure grid independency. Grids containing 28.3 million, 34.97 million, 40.81 million and 81.88 million elements were generated and used in simulations at Reynolds numbers of 670,000 and 917,000. The HTC distribution, total pressure variation over the ribs and random checks of the velocity at various points showed negligible difference for the 40.81 and 81.88 million elements. Therefore, all the simulations are presented using the 40.81 million element mesh. As an example, Table 2 shows the relative deviation of  $Nu_{avg}$ , from the baseline mesh with 40.81 million elements, for different grids on the liquid crystal coated surfaces.

**Table 2: Relative % deviation of  $Nu_{avg}$  for different grids from the 40.81 million element baseline**

% deviation of $Nu_{avg}$ from the baseline case with 40.81 mil elements				
Element count		28.3 mil	34.97 mil	81.88 mil
Re=917K	Seg 3	<15%	~2%	<1%
	Seg 4	~20%	<1%	<1%
Re=670K	Seg 3	<15%	~2%	<1%
	Seg 4	~20%	<2%	<1%

The height of the first layer of cells adjacent to the walls, as evaluated using the  $y^+$  value calculated through Eq. (6), was adjusted to properly capture the viscous sublayer and the heat transfer on the surface. In the mesh used, the  $y^+$  at the wall is always close to or less than unity. A smooth and gradual transition of mesh density is then applied away from the wall. An example of  $y^+$  values for Reynolds number of 917,000 is shown in Fig. 7; indicating a low  $y^+$  value in all areas.

$$y^+ = \frac{\rho u_\tau y_{wall}}{\mu} \quad (6)$$

Where the friction velocity is obtained using Eq. 7.

$$u_\tau = \sqrt{\frac{\tau_w}{\rho}} \quad (7)$$

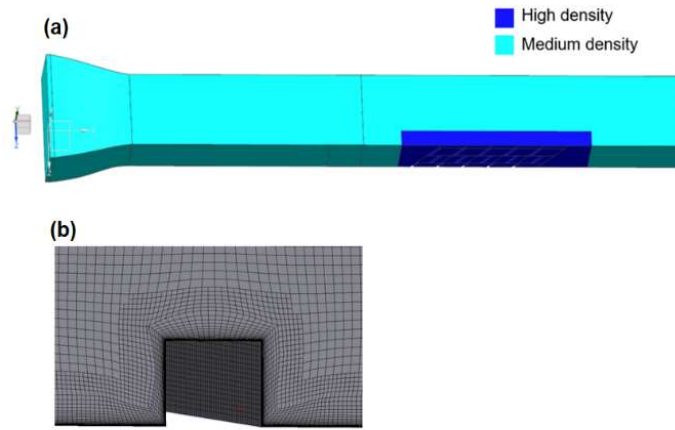


Fig. 6: Division of volume for meshing (a), 3D view of mesh around ribs (b)

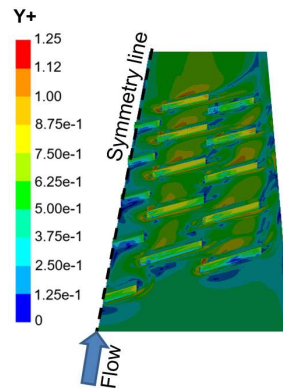


Fig. 7:  $y^+$  distribution for Reynolds number of 917,000

## 5 Results and Discussion

### 5.1 Heat Transfer

Nusselt number ratios, normalized by the Dittus-Boelter correlation at equivalent Reynolds number, over ribbed plates are obtained experimentally and presented in Fig. 8. In this figure, the ribs themselves are shown in white as no heat transfer measurement is available on these surfaces. Figure 8 (a and b) show the contours of the experimentally measured Nusselt number augmentation at Reynolds numbers of 339,000 and 917,000, respectively. The experimental data reveals an increase of the Nusselt number augmentation with Reynolds number, as observed by the increase of the peak Nusselt number areas behind the ribs. However, the overall pattern of the normalized Nusselt number distribution remains the same at all Reynolds numbers, indicating qualitative similarity between flow fields. The larger area of peak Nusselt number ratio at the highest Reynolds number likely indicates higher intensity of turbulence and secondary flow structures emanating from the ribs (Fig. 8). Areas of peak heat transfer correspond to vortical structures which are shed from turbulator extremities and cause boundary layer disruptions downstream. The high lateral variation of the Nusselt number indicates complex 3D disturbances caused by the broken angled ribs. The general qualitative distribution of the CFD estimated Nusselt number agrees with experimental results.

As shown in Fig. 9 and Fig. 10, the overall spatial distribution of the Nusselt number simulated numerically agrees well with experimental measurements, indicating rapid turbulator flow development at high Reynolds numbers. The difference in experimentally measured area weighted averaged Nusselt number ( $Nu_{avg}$ ) between segments 3 and 4 is within 2% at all Reynolds numbers, with similar heat transfer patterns. Small discrepancies could be explained by the rib flow being not fully developed. However, there is a difference in the absolute values of Nusselt number between the experimental and numerical results, with the latter overestimating peak values and underestimating the low areas. Similar behaviour in areas of flow attachment and detachment was reported by Promvonge et al. [16] in their numerical investigation of V shaped broken ribs using the  $\kappa$ - $\epsilon$  RNG turbulence model. The discrepancies between the current numerical and experimental Nusselt number distribution may be attributed to repeated detachment and re-attachment of the flow at each rib, which is not accurately captured by the numerical simulations. In the current investigation, the maximum discrepancy between the numerical and experimental peak Nusselt numbers is observed at the leading edge corner of the most downstream rib segment. Unfortunately, there are no velocity measurements in the current study near the ribs to compare against the numerically estimated velocity profiles. This is due to the current rig set up which does not permit intrusive probes in the region of interest without influencing the turbulator flow field and heat transfer.

The area averaged Nusselt number ratio for segments 3 and 4 is presented in Fig. 10. The normalized area averaged Nusselt number ratio shows a small rise with increasing Reynolds numbers, which is contrary to the results presented by Mhetras et al. [8], Promvonge et al. [16] and Gupta et al. [9]. However, measurements of Nusselt number distribution at additional Reynolds numbers are required to identify a clear trend. This discrepancy may be attributed to the differences, between the current experiment and Ref [8, 9, 16], in channel aspect ratio, turbulator size, channel length and the provisioned gap between the sidewall and the turbulator segment in this investigation. A comparison of the Nusselt number ratio pattern (Fig. 8) with previously published data [9, 11] may shed further light on this discrepancy. These references [9, 11] are selected as detailed normalized Nusselt number contours are presented for the broken V configuration at 60° angle to the flow in a roughly similar channel aspect ratio ( $AR=1$ ). The experimental data [9, 11] indicate that increasing Reynolds number and  $e/D_h$  (from 0.0625 to 0.15) at  $P/e=10$  adversely impacts the Nusselt number ratio downstream (near the base) of the middle rib segment (Fig. 1(a)). In the current experiment (Fig. 8), the corresponding peak Nusselt number ratio area maintains its position and spreads with increasing Reynolds number. Therefore, it is postulated that the lower  $e/D_h$  in the current experiment may have contributed to a sustained axial vortex (emanating from the middle rib segment) that intensifies near the surface with increasing Reynolds number and improves the Nusselt number ratio. In a similar fashion, the Nusselt number ratio between the outer rib segment and the sidewall (Fig. 8) intensifies with Reynolds number, leading to further enhancement of heat transfer augmentation with increasing Reynolds number. In conclusion, a combination of low relative rib height (compared with the works of [9, 11]) and the rib-sidewall gap have likely contributed to the improved heat transfer augmentation with increasing Reynolds number. A direct comparison of the current data and the literature is not possible due to the differences in configurations. However, the normalized experimental Nusselt number values from the current experiments can be considered in the ballpark of the available literature with the deviations attributed to uncertainties around the experimental data and differences in configurations (Fig. 11). The largest discrepancy between the experimental and numerically estimated  $Nu_{avg}$  is observed, Fig. 10, at a Reynolds number of 917,000, where there is a 12.7% difference between the two datasets. The discrepancy is less than 5% for the lower Reynolds numbers, which falls within the uncertainty band of the experiment. Therefore, the only significant underestimation of the  $Nu_{avg}$  occurs at the maximum Reynolds number, where the complex nature of the flow is intensified. The results indicate that the flow development length may be underestimated by the current numerical estimates, especially at  $Re < 917,000$ , as can be seen by the converging numerically estimated Nusselt number ratio lines (on segments 3 and 4) with increasing Reynolds number (Fig. 10). Additionally, the rise in the Nusselt number ratio (with increasing Reynolds number) is not captured by the numerical

estimates. This may be attributed to numerical underestimation of turbulent mixing and convective heat transfer. Since discrepancies between RANS estimates and experimental data were also previously reported in the literature (e.g. Maurer et al. [4, 5]), improved turbulence modelling may be required to better address the root cause of this discrepancy. The area averaged Nusselt number over the ribs was numerically estimated to be between 18% and 30% higher than on the inter-rib surfaces downstream of the corresponding rib set. There is however no experimental data to validate these results. The indication of superior heat transfer on the ribs suggests a significant impact for the rib heat transfer over the global heat transfer, for a wide range of Reynolds numbers. This was also discussed by Maurer et al. [5] in their investigation of continuous V and W ribs and by Taslim and Lengkon [37] for the case of 45° angled turbulators.

To further investigate the discrepancy between the numerical estimates and experimental data at Reynolds number of 917,000, this simulation was repeated with the  $\kappa$ - $\epsilon$  Realizable turbulence model, with enhanced wall treatment. Ieronymidis et al. [27] used this approach for a qualitative study of flow fields around a group of turbulators with no boundary layer mesh on the ribs. The model was again run on both the 40.81 million and the 81.88 million element meshes to ensure grid independency. However, with this model the numerically estimated area averaged Nusselt number and heat transfer coefficient, for inter-rib area in segments 3 and 4, were underpredicted by approximately 35%, a behaviour (underprediction of HTC) also observed by Ieronymidis et al. [27]. Therefore, further simulations were not performed using the  $\kappa$ - $\epsilon$  Realizable turbulence model as the  $\kappa$ - $\omega$  SST provided closer agreement with the experimental data.

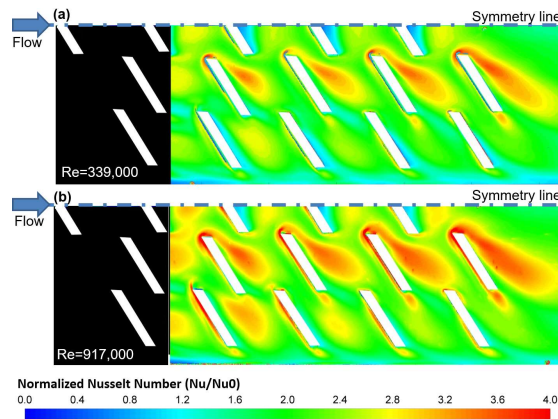


**Fig. 8: Normalized Nusselt ( $Nu/Nu_0$ ) number distribution obtained from experimental data at Reynolds number of 339,000 (a) and Reynolds number of 917,000 (b)**

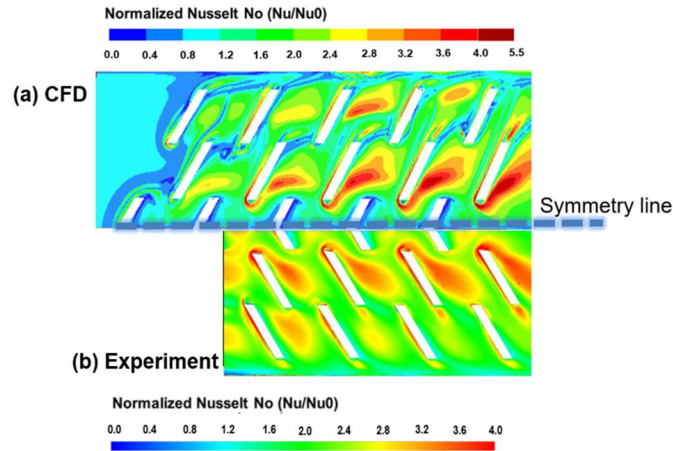


Fig. 9: Numerical (a) and experimental (b) normalized Nusselt number distribution at Reynolds number of 917,000

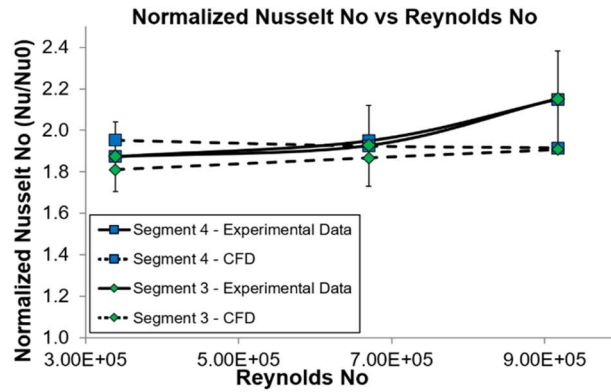


Fig. 10: Area averaged normalized Nusselt number on segments 3 and 4 (excluding ribs)

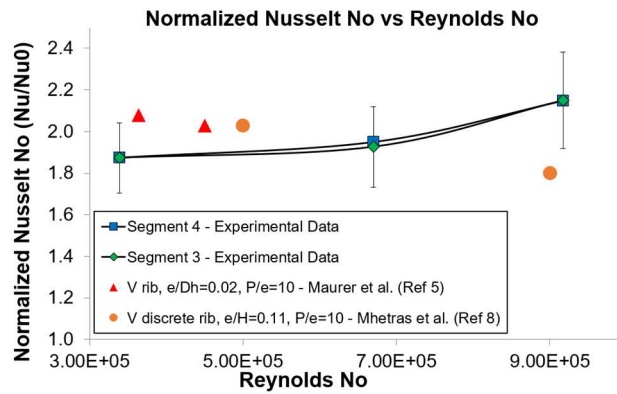


Fig. 11: Comparison of measured normalized Nusselt number with the literature

## 5.2 Flow Structure Discussion Using Numerical Analysis

The flow path lines over the downstream ribs are shown in Fig. 12(a) at Reynolds number of 917,000, allowing comparison with the measured Nusselt number distribution (Fig. 12(b)). In the following, 3 regions featuring interesting flow and heat transfer features will be discussed, represented by labels A, B and C in Fig. 12(a). The 2D cross sections of the velocity vectors, turbulent kinetic energy and vorticity contours, corresponding to these zones are also presented in Fig. 13, Fig. 14 and Fig. 15. These values are normalized by the mass weighted averaged velocity, turbulent kinetic energy and vorticity values in the test section entry region, taken at a distance of one rib spacing upstream of the first rib. In all cases, as the flow reaches the rib, it is deflected upwards and accelerates. This is followed by a sudden expansion downstream where the detachment of the flow leads to recirculation zones at the base of the ribs.

The first region of interest is the head of the chevron in the middle of the plate. A large vortical structure is observed downstream of the rib in the axial direction (Fig. 13(a)). This large vortex causes a low velocity recirculation zone and therefore an area of low Nusselt number. Low turbulent kinetic energy and vorticity levels are also observed in this position immediately downstream of the middle rib in the numerical simulations (Fig. 14(a) and Fig. 15(a)). This low Nusselt number area is also observed in the investigation of Gupta et al. [9]. The poor heat transfer in this region indicates the inability of the vortex to provide improved convective heat transfer between the wall and the core flow. The introduction of a slit in the head of the chevron, corresponding to label Line A in Fig. 12(a), is likely to eliminate or improve the low heat transfer region by allowing longitudinal flow to pass through and wash away the low Nusselt number region.

A second area of interest is the region behind the turbulator segment located slightly downstream of the head of the chevron, labelled B in Fig. 12(a). In this location, the angled rib guides the incoming air and creates a high velocity stream with elevated levels of turbulence intensity, turbulent kinetic energy and vorticity near the surface, leading to an area of elevated heat transfer (Fig. 13(b), Fig. 14(b) and Fig. 15(b)). As the high velocity flow reaches the rib, it climbs over and separates at its sharp corner. The effective area of the channel over the turbulators is therefore further reduced due to the presence of a separation bubble, leading to increased local velocity and turbulence. The centerline of the vortex generated downstream of this rib is at an angle roughly comparable to that of the rib that created it. This strong recirculation zone with a significant axial component is associated with a larger area of intense heat transfer. The effectiveness of this longitudinal secondary flow structure at enhancing heat transfer effect is even more pronounced in the last downstream rib as there is no subsequent rib to deflect it upwards. Qualitatively similar pattern of increased local Nusselt number can be observed in the experiments of SriHarsha et al. [11] for a  $e/D_h$  ratio of 0.0625. However, the data indicates that the normalized Nusselt

number pattern changed noticeably in this region for larger  $e/D_h$  ratios (for attached broken V ribs) due to the deterioration of peak heat transfer augmentation in the downstream vicinity of the rib in this region [11]. The vortical structure in this area also resembles the longitudinal vortices discussed by Fiebig [38], which lead to higher heat transfer near the wall surface compared with transverse vortices. The recirculation of the warmer core flow towards the ribbed walls associated with high angular momentum of the local vortex, thinning of the boundary layer and high local turbulence intensity are likely to be the causes of improved heat transfer in this region. It is noteworthy that the corresponding area on segment 1 shows little improvement of heat transfer in the numerical simulations, as shown in Fig. 9(a). This may be attributed to secondary flow not being sufficiently established and needs to be accounted for if heat transfer in this region is of significance to the design.

A last area of interest is downstream of the turbulator segment adjacent to the side wall, where the flow is guided in a tangential direction towards the solid boundary. Here separation bubble forms over the top surface of the rib (Fig. 13(c)) as was observed in region B. There is no clear significant improvement of heat transfer downstream of the ribs in this region, despite their similarity with those in region B. The normalized vorticity magnitude (Fig. 15(c)) downstream of this rib is also noticeably lower than the equivalent area of region B (Fig. 15(b)). This can be largely attributed to the presence of the side wall, which may lead to a reduction of velocity and turbulence intensity close to the ribbed wall. Low heat transfer near the walls are also observed in the experiments of Gupta et al. [9] and SriHarsha et al. [11], for a slightly different rib geometry. However, a small lobe of high heat transfer augmentation is noticed between the sidewall and the adjacent rib in the current experiment due to the gap between them (Fig. 8 a and b). In this region, the experimentally measured Nusselt number distribution reveals a decrease in heat transfer, compared with the same location in the upstream segments. This may be partially attributed to the evolving interaction of the secondary flow of upstream ribs rolling over the sidewall and into the free stream flow, then adversely affecting the longitudinal vortices near the ribbed surface.

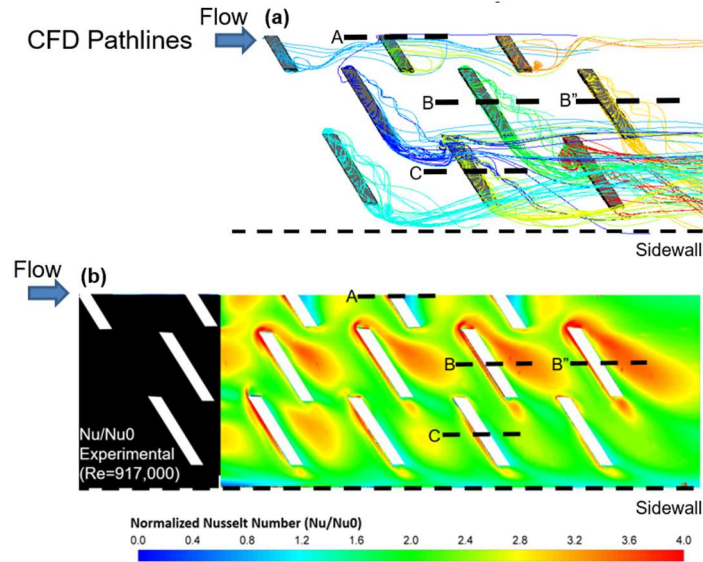


Fig. 12: Flow path lines over downstream ribs. Pathline colours are for providing contrast and improved visualization (a)  
experimental normalized Nusselt number pattern (b)

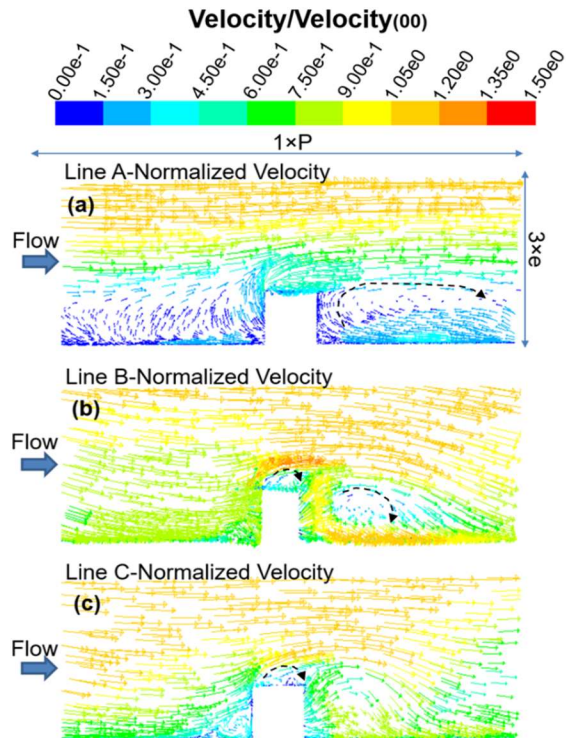


Fig. 13: Normalized velocity at mid sections of rib segments (corresponding to Lines A,B,C in Fig. 12)

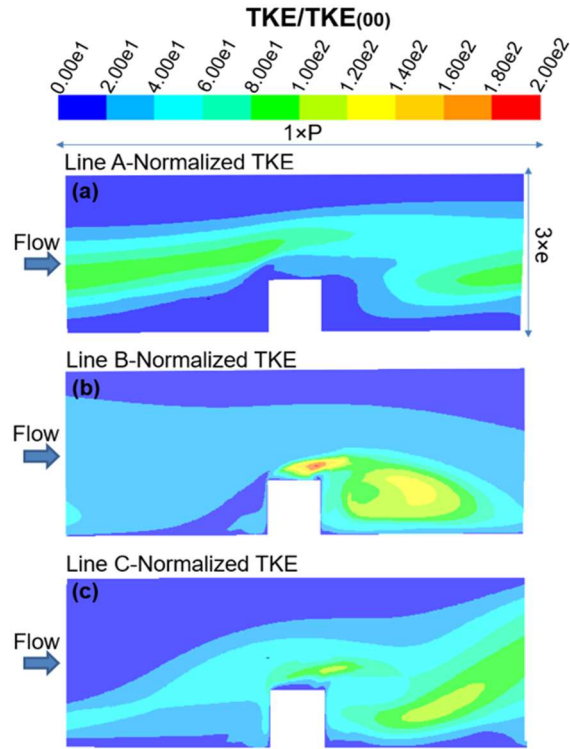


Fig. 14: Normalized TKE at mid sections of rib segments (corresponding to Lines A,B,C in Fig. 12)

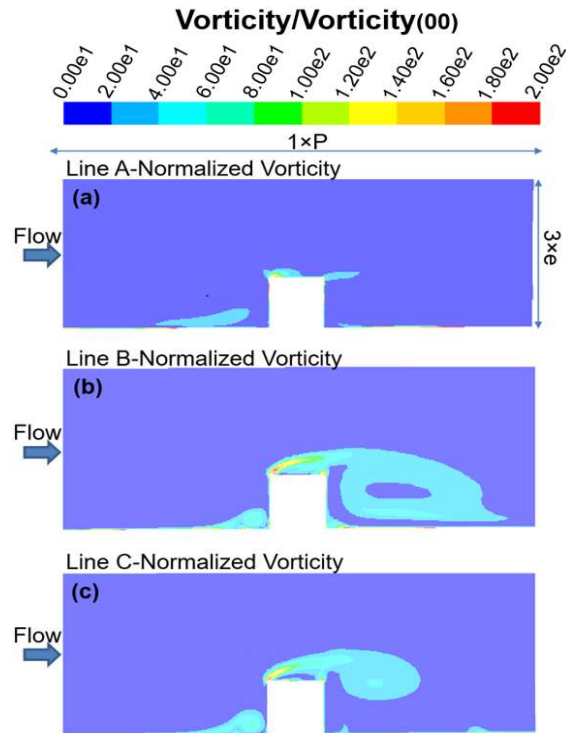


Fig. 15: Normalized vorticity at mid sections of rib segments (corresponding to Lines A,B,C in Fig. 12)

### 5.3 Friction Factor

The pressure losses caused by the ribbed walls are several times higher than those of a smooth channel. This comes as a consequence of the increased skin friction and form drag caused by the additional surface area of the ribbed walls, as well as the existence of protruding features in the flow compared with a smooth channel. As expected, the normalized friction factor, calculated through the Blasius correlation, increases monotonically with increasing Reynolds number (Fig. 16). Interestingly, the pressure loss may be reduced by rounding of the sharp rib corners, as indicated by the experiments of Rallabandi et al. [6] on parallel angled ribs. Qualitative comparison of the measured friction factor from the current experiment indicates a roughly similar slope to that of the continuous V shaped ribs presented by Maurer et al. [5] in a rectangular channel with an aspect ratio of 2:1. As the flow may not be fully developed with the current set up, a longer domain with additional measurements may be required for improved insight.

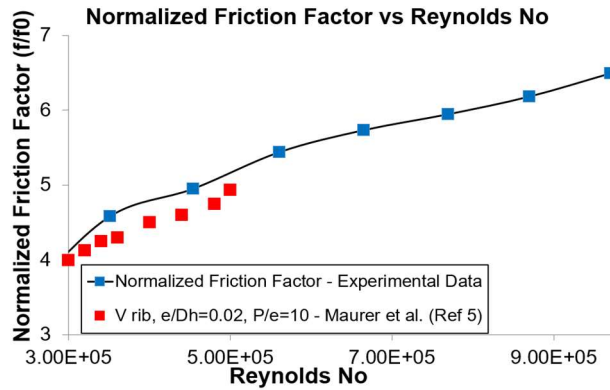
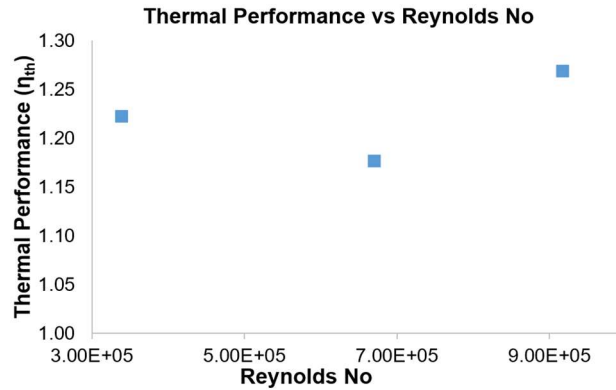


Fig. 16: Normalized friction factor versus Reynolds number (experimental data)

### 5.4 Thermal Performance

Thermal performance (Fig. 17) at constant pumping power using the area weighted averaged Nusselt number over segments 3 and 4 (Fig. 10) and the channel friction factor (Fig. 16) is estimated via the calculation method described in Ref [39, 40] using Eq. (8). The detailed formulation and assumptions for thermal performance calculations are presented by Fan et al. [39].

$$\eta_{th} = \frac{(Nu_{avg}/Nu_0)}{(f/f_0)^{2/7}} \quad (8)$$



**Fig. 17: Thermal performance as a function of Reynolds number (experimental data not including heat transfer over ribs)**

The thermal performance over 1 implies the turbulators (with established secondary flow) provide superior heat transfer compared with a smooth channel at a given pumping power within the examined range of Reynolds numbers, despite the augmentation of the associated friction factor ratio. As discussed previously, a direct comparison of the results with the available literature cannot be made due to differences in turbulator and channel configurations and dimensions. However it is noteworthy that although the thermal performance showed a decline with rising Reynolds number in the data of Maurer et al. [5] (V ribs with  $P/e=10$ ) and Mhetras et al. [8], the current experiment does not indicate a consistent decline of thermal performance with increasing Reynolds number. Additionally, the thermal performance may be further improved by filleting of the ribs similar to the work of Rallabandi et al. [6]. In summary, the current experiment indicates feasibility of achieving thermal performance ( $>1$ ) at elevated Reynolds numbers, however evaluation of thermal performance with additional turbulator rows in a longer channel are required to complement the current experiment. As shown by Promvonge et al. [16] for the case of a broken V turbulator at  $Re=10,000$ , the flow velocity profile and the Nusselt number develop, as the air travels over the rib segments, to exhibit periodic (repeated) characteristics at each segment. For example, in the case of the broken V turbulator at  $e/D_h=0.0625$ , the Nusselt number ratio increases with axial distance before it achieves perfect periodicity [16]. This development length may depend on parameters such as the turbulator configuration,  $e/D_h$  ratio and Reynolds number. Considering the limitations in the current experiment, thermal performance over a larger number of turbulators (requiring a longer channel) should be assessed to examine the impact of further flow development on this parameter.

## 5.5 Traverse Measurements of Pressure Normal to the Flow

Pressure measurements were performed  $1.6 \cdot P$  downstream of the last row of ribs and perpendicular to the flow in unheated conditions. The probe was moved by a traverse mechanism and velocity profiles were then calculated using

Bernoulli's equation. The normalized axial velocity measurements as a function of distance from the ribbed wall are presented in Fig. 18, where line AA is acquired on the symmetry plane and lines BB and CC are  $0.469 \cdot D_h$  and  $0.521 \cdot D_h$  away from the symmetry plane in the lateral direction, respectively (Fig. 19). These traverse lines (AA, BB, CC) were selected for comparison due to the large gradients in their velocity profiles leading to the highest discrepancies between the numerical estimates and experimental data. The profiles cover from the test plate surface (0% channel height) to the top wall (100% channel height), with the velocities normalized by the peak axial velocity on the traverse plane. The profiles obtained from CFD analysis show good qualitative agreement with experimental data away from the ribs. However, the numerical simulations underestimate the axial velocity values and their gradients in close proximity to the ribbed wall. Interestingly, similar plots at Reynolds number of 339,000 did not show a significantly better agreement between the numerical and experimental data, despite the fact that the area averaged Nusselt numbers were shown to be in closer agreement. These plots are not presented for brevity as they follow somewhat similar trends to those shown in Fig. 18. This discrepancy may hint to the inability of the current numerical approach to capture the details of the secondary flow that contributes to the heat transfer distribution over the ribbed wall; as discussed by Forsyth et al. [41] in a similar investigation of turbulator aerodynamics and heat transfer characteristics.

## 5.6 Discussion on Numerical Accuracy

The presented numerical study shows that the current numerical modelling approach can be used as a predictive simulation tool to guide the design of heat transfer enhancing surface features similar to the investigated configuration, but with decreasing accuracy of the model with increasing Reynolds number. Discrepancies between the experimental data and the  $k-\omega$  SST numerically estimated values were also noticed by Tang and Zhu [17] however they were attributed to potential measurement uncertainties and modelling assumptions. Tang and Zhu [17] used sloped ribs which may disrupt the flow more smoothly and avoid large separation. Additionally, their study was performed at Reynolds numbers an order of magnitude lower than the current study and for a different turbulator configuration. We therefore postulate that the current flow may experience a more abrupt separation that poses a challenge for the turbulence model. The use of coarser grid away from the ribs in the entry section (in comparison with the mesh around the ribs) may have also introduced numerical inaccuracies in capturing the flow development at the inlet. However, this inlet effect is not expected to have a significant impact on the numerical results in the downstream segments due to repetitive detachment and attachment of the boundary layer and flow mixing over the ribs, where the mesh is fine.

The numerical approach in the current investigation is unable to capture the flow unsteadiness and the effect of the anisotropic characteristics of turbulence, which may play an important role in the turbulent characteristics of swirling flow and heat transfer near the ribbed walls, as also discussed by Dhopade et al. [36]. It is the opinion of the authors that further evaluation of the various numerical approaches and a sensitivity study of thermal boundary conditions, similar to the works of Lörstad [3] and Iaccarino et al. [42], would be beneficial for a comprehensive numerical capability assessment. Additionally, detailed flow measurements (i.e. velocity and temperature) near the ribbed surface are required for the detailed validation of numerical results.

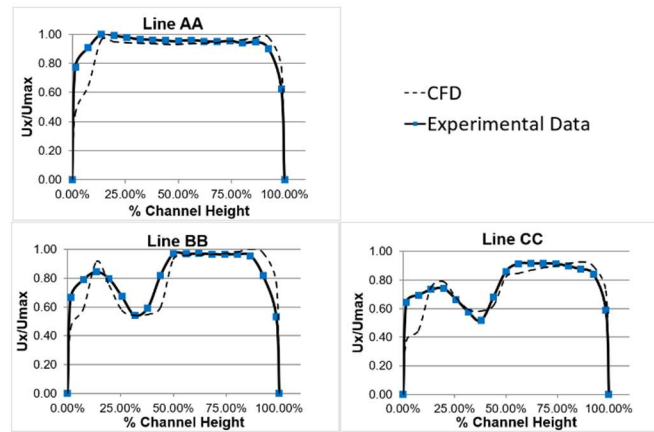


**Fig. 18: Normalized axial velocity vs distance from ribbed wall at  $Re=950,000$**

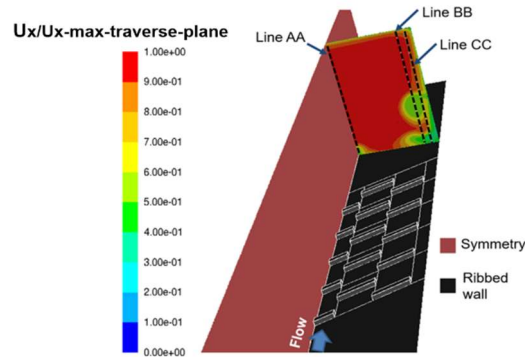


**Fig. 19: Numerically estimated normalized axial velocity profile on traverse plane ( $Re=950,000$ )**

## 6 Conclusion

The Nusselt number distribution and pressure drop over 10 rows (5 segments) of broken V ribs were studied both numerically and experimentally at Reynolds numbers between 339,000 and 917,000. High resolution heat transfer measurements were performed using transient liquid crystal thermography. The flow characteristics and heat transfer coefficient of the turbulator plate was investigated numerically via the  $\kappa$ - $\omega$  SST turbulence model using the commercial software platform, ANSYS Fluent®.

The experimental data indicates an average heat transfer enhancement ratio between 1.87 to 2.15, at Reynolds numbers between 339,000 and 917,000, on the inter-rib surfaces where secondary flow is established. Here a thermal performance value above 1 indicates that the investigated ribbed surface provides enhanced heat transfer compared with a smooth channel at a constant pumping power. The friction factor ratio of the ribbed channel is more than 6 times that of a smooth channel at  $Re \approx 900,000$ . A small lobe of peak Nusselt number ratio forms between the sidewall and the rib that intensifies with increasing Reynolds number.

Both experimental and numerical results reveal an area of low heat transfer immediately downstream of the apex of V shaped ribs, on the symmetry line. Breaking of the rib at its apex and rounding of the ribs' sharp corners are likely to improve the heat transfer and potentially reduce the pressure losses. The highest heat transfer was observed downstream of the rib segments located between the apex of the chevron and its outermost leg segment where peak levels of near ribbed-wall velocity, turbulent kinetic energy and vorticity were indicated by the numerical computations.

Both heat transfer and friction factor augmentations increased with rising Reynolds number. The results demonstrate the effectiveness of turbulators for enhancement of heat transfer for a wide range of Reynolds numbers. Although the numerical simulations provide insight into the global characteristics of the flow, discrepancies were observed with experimental data, especially at high Reynolds numbers. Measurements of flow velocity and temperature profile at and between the ribs are recommended for a detailed investigation of flow features.

## Acknowledgement

The authors are grateful to Siemens Energy Canada for supporting this research and permission to report this investigation. Additionally, the authors thank their colleagues who have helped with this investigation. Computing resource at Polytechnique Montréal was kindly supported via NSERC Discovery Grant RGPIN-2014-03622.

## Permission for Use

The content of this paper is copyrighted by Siemens Energy Canada Limited and is licensed to ASME for publication and distribution only. Any inquiries regarding permission to use the content of this paper, in whole or in part, for any purpose must be addressed to Siemens Energy Canada Limited directly.

## Nomenclature

A	[m <sup>2</sup> ]	area
D <sub>h</sub>	[m]	channel hydraulic diameter
e	[m]	rib height
f	-	friction factor
H	[m]	channel height
HTC (h)	[W/(m <sup>2</sup> .K)]	Heat Transfer Coefficient
k <sub>air</sub>	[W/(m.K)]	air thermal conductivity
Nu	-	Nusselt number
P	[m]	rib pitch
Pr	-	air Prandtl number $\approx 0.7$
$\dot{Q}$	[W]	heat flux
$Re_{Dh} = \frac{\rho u D_h}{\mu}$	-	Reynolds number
T <sub>ref-air</sub>	[K]	reference air temperature
T <sub>wall</sub>	[K]	wall temperature
T <sub>inlet-air</sub>	[K]	inlet air temperature
$\Delta T$	[K]	T <sub>air</sub> - T <sub>wall</sub>
TKE	[m <sup>2</sup> /s <sup>2</sup> ]	turbulent kinetic energy $0.5(\overline{u'^2_x} + \overline{u'^2_y} + \overline{u'^2_z})$
$\eta_{th}$	-	thermal performance at constant pumping power
u	[m/s]	velocity
u'	[m/s]	velocity fluctuation
W	[m]	channel width

$W/H$	-	channel aspect ratio
$y_{wall}$	[m]	distance from wall

### Greek Symbols

$\rho$	[kg/m <sup>3</sup> ]	air density
$\mu$	[kg/(m.s)]	air dynamic viscosity
$\tau$	[Pa]	shear stress

### Subscripts

0	evaluated for a smooth channel
00	refers to values at a distance of one pitch upstream of first rib
avg	area averaged
max-traverse-plane	denoting maximum value on traverse plane
x,y,z	represent x,y,z directions in Cartesian coordinates

### References

- [1] Tamna, S., Kaewkohkiet, Y., Skullong, S., and Promvonge, P., 2016, "Heat Transfer Enhancement in Tubular Heat Exchanger with Double V-Ribbed Twisted-Tapes," Case Stud. Therm. Eng., 7, pp. 14-24.
- [2] Hagari, T., Ishida, K., Oda, T., Douura, Y., and Kinoshita, Y., 2011, "Heat Transfer and Pressure Losses of W-Shaped Small Ribs at High Reynolds Numbers for Combustor Liner," ASME J. Eng. Gas Turb. Power, 133(9).
- [3] Lörstad, D., 2012, "LES and RANS Assessment of Rib Cooled Channel Related to SGT-800 Combustor Liner," ASME Paper No. GT2011-46415.
- [4] Maurer, M., von Wolfersdorf, J., and Gritsch, M., 2007, "An Experimental and Numerical Study of Heat Transfer and Pressure Loss in a Rectangular Channel with V-Shaped Ribs," ASME J. Turbomach, 129(4), pp. 800-808.
- [5] Maurer, M., von Wolfersdorf, J., and Gritsch, M., 2007, "An Experimental and Numerical Study of Heat Transfer and Pressure Losses of V- and W-Shaped Ribs at High Reynolds Numbers," ASME Paper No. GT2007-27167.
- [6] Rallabandi, A. P., Alkhamis, N., and Han, J. C., 2011, "Heat Transfer and Pressure Drop Measurements for a Square Channel With 45 deg Round-Edged Ribs at High Reynolds Numbers," ASME J. Turbomach, 133(3), p. 031019.
- [7] Zhang, M., Singh, P., and Ekkad, S. V., 2019, "Rib Turbulator Heat Transfer Enhancements at Very High Reynolds Numbers," ASME J. Therm. Sci. Eng. Appl., 11(6), p. 061014.

- [8] Mhetras, S., Han, J. C., and Huth, M., 2014, "Heat Transfer and Pressure Loss Measurements in a Turbulated High Aspect Ratio Channel With Large Reynolds Number Flows," ASME J. Therm. Sci. Eng. Appl., 6(4), p. 041001.
- [9] Gupta, A., SriHarsha, V., Prabhu, S. V., and Vedula, R. P., 2008, "Local Heat Transfer Distribution in a Square Channel with 90° Continuous, 90° Saw Tooth Profiled and 60° Broken Ribs," Exp. Therm. Fluid Sci., 32(4), pp. 997-1010.
- [10] Han, J. C., and Zhang, Y. M., 1992, "High Performance Heat Transfer Ducts with Parallel Broken and V-Shaped Broken Ribs," Int. J. Heat Mass Transfer, 35(2), pp. 513-523.
- [11] SriHarsha, V., Prabhu, S. V., and Vedula, R. P., 2009, "Influence of Rib Height on the Local Heat Transfer Distribution and Pressure Drop in a Square Channel with 90° Continuous and 60° V-Broken Ribs," Appl. Therm. Eng., 29(11-12), pp. 2444-2459.
- [12] Kiml, R., Mochizuki, S., and Murata, A., 2001, "Effects of Rib Arrangements on Heat Transfer and Flow Behavior in a Rectangular Rib-Roughened Passage: Application to Cooling of Gas Turbine Blade Trailing Edge," ASME J. Heat Trans., 123(4), pp. 675-681.
- [13] Han, J. C., Ou, S., Park, J. S., and Lei, C. K., 1989, "Augmented Heat Transfer in Rectangular Channels of Narrow Aspect Ratios with Rib Turbulators," Int. J. Heat Mass Transfer, 32(9), pp. 1619-1630.
- [14] Han, J. C., Park, J. S., and Lei, C. K., 1985, "Heat Transfer Enhancement in Channels With Turbulence Promoters," ASME J. Eng. Gas Turb. Power, 107(3), pp. 628-635.
- [15] Han, J. C., and Park, J. S., 1988, "Developing Heat Transfer in Rectangular Channels with Rib Turbulators," Int. J. Heat Mass Transfer, 31(1), pp. 183-195.
- [16] Promvonge, P., Changcharoen, W., Kwankaomeng, S., and Thianpong, C., 2011, "Numerical Heat Transfer Study of Turbulent Square-Duct Flow Through Inline V-Shaped Discrete Ribs," Int. Commun. Heat Mass Trans., 38(10), pp. 1392-1399.
- [17] Tang, X. Y., and Zhu, D. S., 2013, "Flow Structure and Heat Transfer in a Narrow Rectangular Channel with Different Discrete Rib Arrays," Chem. Eng. Process., 69, pp. 1-14.
- [18] Versteeg, H. K., and Malalasekera, W., 2007, "An Introduction to Computational Fluid Dynamics: the Finite Volume Method," 2nd ed., Pearson Education Ltd., U.K, pp. 97-98.
- [19] Choi, E. Y., Choi, Y. D., Lee, W. S., Chung, J. T., and Kwak, J. S., 2013, "Heat Transfer Augmentation Using a Rib-Dimple Compound Cooling Technique," Appl. Therm. Eng., 51(1-2), pp. 435-441.

- [20] Chaube, A., Sahoo, P. K., and Solanki, S. C., 2006, "Analysis of Heat Transfer Augmentation and Flow Characteristics Due to Rib Roughness Over Absorber Plate of a Solar Air Heater," *Renew. Energy*, 31(3), pp. 317-331.
- [21] Han, J. C., Dutta, S., and Ekkad, S. V., 2000, *Gas Turbine Heat Transfer and Cooling Technology*, Taylor & Francis, U.S.A.
- [22] Ghorbani-Tari, Z., Sunden, B., and Tanda, G., 2011, "On Liquid Crystal Thermography for Determination of the Heat Transfer Coefficient in Rectangular Ducts," *Proc. 15th Int. Conf. on Computational Methods and Experimental Measurements*, pp. 255-266.
- [23] Ireland, P. T., and Jones, T. V., 2000, "Liquid Crystal Measurements of Heat Transfer and Surface Shear Stress," *Meas. Sci. Technol.*, pp. 969-986.
- [24] Clifford, R. J., Jones, T. V., and Dunne, S. T., 1983, "Techniques for Obtaining Detailed Heat Transfer Coefficient Measurements Within Gas Turbine Blade and Vane Cooling Passages," *ASME Paper No. 83-GT-58*.
- [25] Byerley, A. R., Jones, T. V., and Ireland, P. T., 1992, "Internal Cooling Passage Heat Transfer Near the Entrance to a Film Cooling Hole: Experimental and Computational Results," *ASME Paper No. 92-GT-241*.
- [26] Munson, B. R., Young, D. F., and Okiishi, T. H., 2006, *Fundamentals of Fluid Mechanics*, 5th ed., John Wiley and Sons, U.S.A, pp. 405-406.
- [27] Ieronymidis, I., Gillespie, D. R. H., Ireland, P. T., and Kingston, R., 2006, "The Use of High Blockage Ribs to Enhance Heat Transfer Coefficient Distributions in a Model of an Integrally Cast Cooling Manifold," *ASME Paper No. GT2006-91237*.
- [28] Ryley, J. R., McGilvray, M., and Gillespie, D., 2019, "Local Heat Transfer Coefficient Measurements on an Engine-Representative Internal Cooling Passage," *J. Thermophys. Heat Trans.*, 33(1), pp. 189-198.
- [29] McGilvray, M., and Gillespie, D., 2011, "Transient Heat Transfer Analysis Code for Liquid Crystal Experiments at the University of Oxford: Updated GUI Driven Software," University of Oxford, Oxford, U.K.
- [30] Ireland, P. T., Neely, A. J., Gillespie, D. R. H., and Robertson, A. J., 1999, "Turbulent Heat Transfer Measurements Using Liquid Crystals," *Int. J. Heat Fluid Flow*, 20(4), pp. 355-367.
- [31] Tsang, C. L. P., 2002, "High Blockage Turbulators in Gas Turbine Cooling Passages," Ph.D Dissertation, University of Oxford, Oxford, U.K.
- [32] Byerley, A. R., 1989, "Heat Transfer Near the Entrance to a Film Cooling Hole in a Gas Turbine Blade," Ph.D Dissertation, University of Oxford, Oxford, U.K.

- [33] Moffat, R. J., 1982, "Contributions to the Theory of Single-Sample Uncertainty Analysis," ASME J. Fluid Eng., 104, pp. 250-260.
- [34] Menter, F. R., 1993, "Zonal Two Equation  $k-\omega$  Turbulence Models for Aerodynamic Flows," AIAA Paper No. 93-2906.
- [35] ANSYS, 2016, ANSYS FLUENT® Release 17.1.0 *Theory Guide*, ANSYS, Inc., U.S.A.
- [36] Dhopade, P., Capone, L., McGilvray, M., Gillespie, D., and Ireland, P., 2015, "Numerical Modelling Techniques for Turbine Blade Internal Cooling Passages," ASME Paper No. GT2015-42393.
- [37] Taslim, M. E., and Lengkon, A., 1998, "45° Round-Corner Rib Heat Transfer Coefficient Measurements in a Square Channel," ASME Paper No. 98-GT-176.
- [38] Fiebig, M., 1995, "Embedded Vortices in Internal Flow: Heat Transfer and Pressure Loss Enhancement," Int. J. Heat Fluid Flow, 16(5), pp. 376-388.
- [39] Fan, J. F., Ding, W. K., Zhang, J. F., He, Y. L., and Tao, W. Q., 2009, "A Performance Evaluation Plot of Enhanced Heat Transfer Techniques Oriented for Energy-Saving," Int. J. Heat Mass Transfer, 52(1-2), pp. 33-44.
- [40] Kunstmann, S., von Wolfersdorf, J., and Ruedel, U., 2010, "Heat Transfer and Pressure Drop in Combustor Cooling Channels with Combinations of Geometrical Elements," ASME Paper No. GT2010-23234.
- [41] Forsyth, P., McGilvray, M., and Gillespie, D. R. H., 2017, "Secondary Flow and Heat Transfer Coefficient Distributions in the Developing Flow Region of Ribbed Turbine Blade Cooling Passages," Exp. Fluids, 58(1).
- [42] Iaccarino, G., Ooi, A., Durbin, P. A., and Behnia, M., 2002, "Conjugate Heat Transfer Predictions in Two-Dimensional Ribbed Passages," Int. J. Heat Fluid Flow, 23(3), pp. 340-345.

## List of tables

Table 1: Test configuration.....	8
Table 2: Relative % deviation of $Nu_{avg}$ for different grids from the 40.81 million element baseline.....	14

## List of figures

Fig. 1: Rib arrangement, angle, and height (a) geometric dimensions (b) .....	8
Fig. 2: Geometrical segments used for discussion and heat transfer averaging .....	8
Fig. 3: Wind tunnel arrangement (a), bell mouthed inlet (b), heater mesh (c).....	9
Fig. 4: Camera position outside of rig (a) view of test section from outside while heater mesh is turned on (b) .....	9
Fig. 5: Boundaries.....	13
Fig. 6: Division of volume for meshing (a), 3D view of mesh around ribs (b).....	15
Fig. 7: $y^+$ distribution for Reynolds number of 917,000.....	15
Fig. 8: Normalized Nusselt ( $Nu/Nu_0$ ) number distribution obtained from experimental data at Reynolds number of 339,000 (a) and Reynolds number of 917,000 (b) .....	18
Fig. 9: Numerical (a) and experimental (b) normalized Nusselt number distribution at Reynolds number of 917,000..	19
Fig. 10: Area averaged normalized Nusselt number on segments 3 and 4 (excluding ribs).....	19
Fig. 11: Comparison of measured normalized Nusselt number with the literature .....	19
Fig. 12: Flow path lines over downstream ribs. Pathline colours are for providing contrast and improved visualization (a) experimental normalized Nusselt number pattern (b) .....	22
Fig. 13: Normalized velocity at mid sections of rib segments (corresponding to Lines A,B,C in Fig. 12) .....	22
Fig. 14: Normalized TKE at mid sections of rib segments (corresponding to Lines A,B,C in Fig. 12) .....	23
Fig. 15: Normalized vorticity at mid sections of rib segments (corresponding to Lines A,B,C in Fig. 12) .....	23
Fig. 16: Normalized friction factor versus Reynolds number (experimental data).....	24
Fig. 17: Thermal performance as a function of Reynolds number (experimental data not including heat transfer over ribs) .....	25
Fig. 18: Normalized axial velocity vs distance from ribbed wall at $Re=950,000$ .....	27
Fig. 19: Numerically estimated normalized axial velocity profile on traverse plane ( $Re=950,000$ ) .....	27